Briefings in Bioinformatics, 2026, 27, bbag060
https://doi.org/10.1093/bib/bbag060
Published: 13 February 2026
Problem Solving Protocol

OXFORD

3D reconstruction of spatial transcriptomics with spatial pattern enhanced graph convolutional neural network

Chen Tang[1,‡], Yuansheng Zhou[1,‡], Xue Xiao[1,‡], Lei Dong[1], Lei Yu[1], Qiwei Li[2], Guanghua Xiao[1,3,*], Lin Xu[1,4,*]

[1]Quantitative Biomedical Research Center, Department of Health Data Science & Biostatistics, Peter O'Donnell Jr. School of Public Health, University of Texas Southwestern Medical Center, 5323 Harry Hines Blvd., Dallas, TX 75390, United States
[2]Department of Mathematical Sciences, The University of Texas at Dallas, 800 W. Campbell Road, Richardson, Texas 75080-3021, United States
[3]Department of Bioinformatics, University of Texas Southwestern Medical Center, 5323 Harry Hines Blvd., Dallas, TX 75390, United States
[4]Department of Pediatrics, Division of Hematology/Oncology, University of Texas Southwestern Medical Center, 5323 Harry Hines Blvd., Dallas, TX 75390, United States

*Corresponding authors. Lin Xu, Quantitative Biomedical Research Center, Department of Health Data Science & Biostatistics, Peter O'Donnell Jr. School of Public Health, University of Texas Southwestern Medical Center, 5323 Harry Hines Blvd., Dallas, TX 75390, United States. E-mail: Lin.Xu@UTSouthwestern.edu; Guanghua Xiao, Quantitative Biomedical Research Center, Department of Health Data Science & Biostatistics, Peter O'Donnell Jr. School of Public Health, University of Texas Southwestern Medical Center, 5323 Harry Hines Blvd., Dallas, TX 75390, United States. E-mail: Guanghua.Xiao@UTSouthwestern.edu
‡Chen Tang, Yuansheng Zhou, and Xue Xiao contributed equally to this work.

Abstract

Spatially resolved transcriptomics (SRT) is a promising new technology that enables simultaneous analysis of gene expression and spatial information for biomedical research. However, the existing statistical and deep learning algorithms used for analyzing SRT data rely solely on two-dimensional (2D) spatial coordinates, which limits their ability to accurately identify spatial domains, spatially variable genes (SVGs), cell-to-cell communications, and developmental trajectories in a three-dimensional (3D) spatial manner. To address these limitations, we introduced Spa3D, which utilized the anti-leakage Fourier transform and graph convolutional neural network model to reconstruct 3D-based spatial structures from multiple 2D SRT slices. We demonstrate that Spa3D is appliable to analyze data from various SRT technology platforms and outperforms state-of-art methods by: (i) improving spatial domain identification through 3D reconstruction, (ii) elucidating cell–cell communication landscape in the 3D cellular organization, (iii) modeling of organ-level tempo-spatial development patterns in a 3D fashion, and (iv) annotating 3D spatial trajectory that are not captured by 2D spatial coordinates.

Keywords spatial transcriptomics, 3D reconstruction algorithm, graph convolutional network, spatial pattern enhancement

Introduction

Single-cell transcriptomics (scRNA-seq) has revolutionized biomedical research, enabling exploration of gene expression at the individual cell level. However, most scRNA-seq protocols destroy spatial context information that offers insights into tissue organization, cell–cell communication, and microenvironment [1, 2]. To address this, spatially resolved transcriptomics (SRTs) technologies [2–7] integrate gene expression with two-dimensional (2D) spatial coordinates. This approach for biomedical studies [1, 2] creates an urgent need for computational methods that incorporate both 2D and three-dimensional (3D) spatial information into SRT data analysis to understand biological processes in tissue morphology.

Why do we need 3D information for spatial transcriptomics? Most biological processes occur in 3D tissue structures that enable cell–cell interactions, communication, and specialized microenvironments. A single 2D slice cannot capture these complex 3D relationships. For example, a liver cross-section may intersect tubular central veins at varying angles, producing different lumen shapes. Thus, understanding spatial dynamics and interactions in 3D is essential for fully interpreting biological function.

Advances in statistics and deep learning have offered insights into SRT data—identifying spatial domains [8–10], cell–cell communication [11–16], and developmental trajectories [17–22]. However, these computational algorithms [8–23] rely on 2D coordinates, preventing them from leveraging true 3D organization. For instance, SpaGCN [8] combined gene expression with image data for spatial clustering but only used 2D coordinates. Additionally, methods such as CellPhoneDB [11], CellChat [12], and NicheNet [13] were designed for single-cell RNA-seq. Newer tools for SRT (e.g. SpaTalk [14], COMMOT [15], and NCEM[16]) also limit themselves to 2D spatial coordinates without incorporating 3D interaction information. Similarly, existing pseudotime and trajectory analysis methods either omit spatial information [18–22], or only leverage 2D coordinates [17]. These limitations motivate the need for algorithms that exploit 3D data to define spatial domains,

Received: June 3, 2025. **Revised:** January 12, 2026. **Accepted:** January 23, 2026

cell–cell communication networks, and developmental trajectories, thereby maximizing SRT's potential.

PASTE [24] is a leading method for aligning multiple 2D SRT slices in 3D. It offers two modes: pairwise slice alignment, which stacks slices without reconstructing true 3D gene expression, and center slice integration, which merges data into a single 2D 'center' slice—sacrificing 3D resolution. PASTE has three major limitations. First, its 'center slice' provides only a 2D overview rather than a genuine 3D reconstruction, so it cannot deliver slice-specific 3D clustering or trajectory information. Second, PASTE ignores real z-axis distances between adjacent slices, preventing accurate 3D layout reconstruction. This issue also affects other integration methods such as DeepST [25] and BASS [26], which use deep learning or Bayesian models for segmentation instead of explicit 3D reconstruction. Third, PASTE assumes that adjacent 2D slices are highly similar, which often fails on real datasets where neighboring sections differ.

To overcome these challenges, we developed Spa3D, a graph-convolutional neural network (GCN) for 3D reconstruction from multiple 2D SRT slices that explicitly incorporates true z-axis distances, enabling more accurate 3D reconstructions than PASTE. By using actual x-, y-, and z-axis coordinates, Spa3D constructs a genuine 3D structure rather than relying on a 2D 'center slice.' We applied Spa3D to various SRT platforms (e.g. 10x Genomics Visium, ST, Stereo-seq, and MERFISH) and found that it can (i) improve spatial domain identification, (ii) reveal detailed 3D cell–cell communication networks, (iii) map organ-level temporal and spatial development in 3D, and (iv) identify 3D spatial trajectories that are invisible in 2D. Overall, Spa3D provides a fuller 3D picture of cellular organization and development, with significant implications for biomedical research and clinical applications.

Results

Overview of Spa3D

Figure 1A illustrates the overall workflow of Spa3D, which integrates consecutive multi-slice 2D spatial transcriptomics (SRT) datasets for 3D reconstruction and downstream analyses. Each 2D SRT dataset is first processed using either the Hilbert transform or the anti-leakage transform to extract coherent spatial signals and suppress noise, thereby enhancing biologically meaningful spatial features within individual slices prior to alignment or graph learning. The enhanced 2D omics datasets are then aligned to correct inter-slice deviations and generate aligned spatial coordinates (x',y'). After alignment, z-coordinates are assigned to each slice based on their physical or sequential order. The aligned (x,'y') coordinates and assigned z-positions are combined to construct a 3D adjacency matrix that encodes spatial relationships among all points across slices and modalities, capturing both local 2D neighborhood structure and inter-slice proximity. This adjacency matrix, together with node features from all enhanced omics, is subsequently input into a GCN. The GCN learns low-dimensional embeddings, which are further refined through a Deep Embedded Clustering (DEC)-based optimization using soft cluster assignments. In this way, the GCN model integrates molecular and spatial information to produce spatially coherent tissue domains. Collectively, Spa3D outputs 3D spatial domain maps, aligned and denoised multi-omics feature matrices, and learned embeddings, which support diverse downstream analyses such as spatial domain identification, pseudotime inference, cell–cell communication and 3D spatial trajectory (Fig. 1B).

Human dorsolateral prefrontal cortex dataset by 10x genomics Visium platform

To compare Spa3D with PASTE, we applied Spa3D to the human dorsolateral prefrontal cortex (DLPFC) dataset [27], previously used to showcase the capability of PASTE in 3D spatial domain identification [24]. This 10x Genomics Visium dataset uses curated annotations from the original study [27] as ground truth.

First, to assess spatial-domain identification, we compared Spa3D and PASTE using the adjusted Rand Index (ARI). A higher ARI indicates closer agreement with the curated annotations [27]. In the original PASTE publication [24], PASTE established stacked 3D alignment and integrated multiple SRT slices of DLPFC samples into a single "center slice" using optimal transport formulation. In contrast, Spa3D characterizes the detailed 3D cellular organization in each individual SRT slice without the need to establish a single 2D-based "center slice." Across all DLPFC slices in the 3D spatial reconstruction, Spa3D achieved an ARI score of 0.62 for the whole 3D spatial structure as depicted in Fig. 2A. Because the Spa3D directly presented the 3D structure while the PASTE method only provided a summarized 2D 'center slice' to represent all the slices, for a fair comparison purpose, we compared the 2D 'center slice' (ARI = 0.53, Fig. 2B) with the corresponding 2D slice from Spa3D reconstruction (ARI = 0.63, Fig. 2B), instead of comparing with the whole Spa3D-defined 3D reconstruction in Fig. 2A. It is important to note that all of the Spa3D-reconstructed individual slices (ARI from 0.58 to 0.63) (Supplementary Fig. 1) outperformed the PASTE-defined 'center slice' in clustering accuracy, not just the one showcased in Fig. 2B.

To understand whether utilizing 3D spatial reconstruction via Spa3D will improve 2D-based spatial domain analysis, we compared its performance with that of SpaGCN, the state-of-the-art spatial domain segmentation algorithm for 2D SRT data. While Spa3D-defined spatial domains and curated annotations shared the same layer or domain structures, SpaGCN-defined spatial domains missed a true layer (green in the curated annotation figure) and introduced an artificial layer (grey in the SpaGCN figure) that did not match with the curated annotations (ARI = 0.43, Fig. 2B). Additionally, we observed several inconsistencies between PASTE-defined spatial domains and curated annotations, including a missing layer (green in the annotation figure) and a wrongly annotated layer (grey in the PASTE figure) that did not exist in the annotation figure, both of which negatively impacted its clustering accuracy (Fig. 2B). These results show that Spa3D outperforms other methods in identifying spatial domains and that using 3D reconstruction improves domain segmentation. Besides SpaGCN and PASTE, we also compared Spa3D to another two competing methods STAGATE and GraphST in Supplementary Fig. 2 and showed that Spa3D achieves the highest ARI.

To examine whether the identified domains from Spa3D are biologically meaningful, we extracted spatial domain associated spatially variable genes (sdaSVGs), which were defined previously [8] by differential expression analysis among different spatial domains. To achieve a reliable and robust conclusion, we applied two most commonly used approaches, edgeR [28] and Seurat [29] packages, to present the results of differential expression analysis on the seven layers (L1 – L6 and WM) of the prefrontal cortex (Supplementary Fig. 3). We compared Spa3D with PASTE in identifying sdaSVGs of each of the seven layers in Fig. 2A and identified sdaSVGs overlap with the known dorsolateral prefrontal cortex gene set from the Allen Mouse Brain Atlas [30]. Our analysis revealed that, in the majority of comparisons,

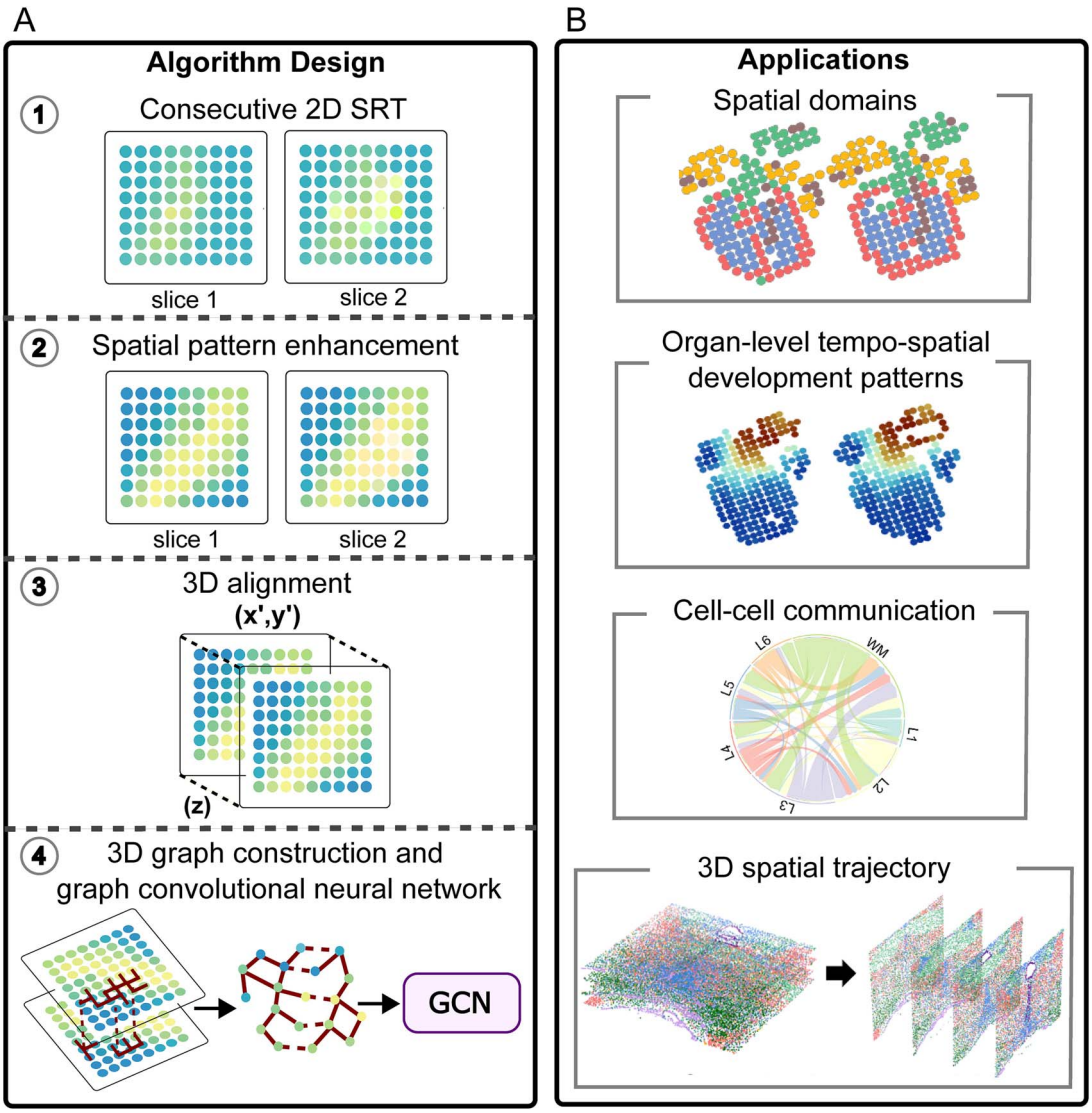

Figure 1 Overview of the Spa3D workflow and its applications. (A) The schematic of Spa3D workflow which comprises several key steps. First, multiple consecutive 2D spatial transcriptomics (SRT) slices are collected as input. Second, each slice undergoes spatial pattern enhancement using the Hilbert transform or the anti-leakage Fourier transform (ALFT) algorithm to extract coherent spatial features and suppress noise. Third, the spatial coordinates are aligned with the techniques implemented in PASTE if the aligned coordinates are not available. After assigning z-coordinates based on slice order, a 3D graph network is constructed to capture both intra- and inter-slice spatial relationships. The graph and molecular features are then input into a graph convolutional network (GCN) trained with a DEC-inspired clustering strategy to generate integrated embeddings and spatially coherent tissue domains. (B) The four major applications of Spa3D: identification of spatial domains, elucidation of organ-level tempo-spatial developmental patterns in three dimensions, mapping of cellular communication landscapes, and discovery of 3D spatial trajectories.

Spa3D-defined sdaSVGs are more enriched of known dorsolateral prefrontal cortex genes than PASTE-defined sdaSVGs, as indicated by both edgeR (Supplementary Fig. 3A) and Seurat (Supplementary Fig. 3B) approaches. This consistency between two distinct differential expression analysis methods suggests that the spatial domains and domain-specific expressed genes identified by Spa3D are more biologically meaningful and consistent with existing knowledge than PASTE. Overall, our results demonstrate the consistent superiority of Spa3D in detecting spatial domains and sdaSVGs.

Second, we evaluated whether Spa3D-derived pseudotime could be more accurate than pseudotime inferred based on PASTE and SpaGCN (Fig. 2C). Across all four SRT slices, Spa3D-derived pseudotemporal structure corresponds to the well-established "inside-out" layer pattern of corticogenesis [31, 32]: new neurons are born in the ventricular zone, migrate along the radial glia fibers in a vertical fashion towards the marginal zone. Therefore, Spa3D's pseudotime accurately reflects the dorsolateral prefrontal cortex's layered organization, whereas PASTE and SpaGCN fail to capture the inside-out sequence of cortical layer development. This highlights how Spa3D's 3D reconstruction improves pseudotime inference, offering deeper insights into the molecular mechanisms of development and disease.

Third, we investigated whether Spa3D could accurately identify ligand-receptor signaling pathways involved in cell–cell communication, in comparison with PASTE and SpaGCN (Fig. 2D and E). To robustly define cell–cell communication, we employed two distinct frameworks, LIANA [33] and SpaTalk [14]. The LIANA package comprises several most frequently used cell–cell communication analysis algorithms that were originally designed for scRNAseq data

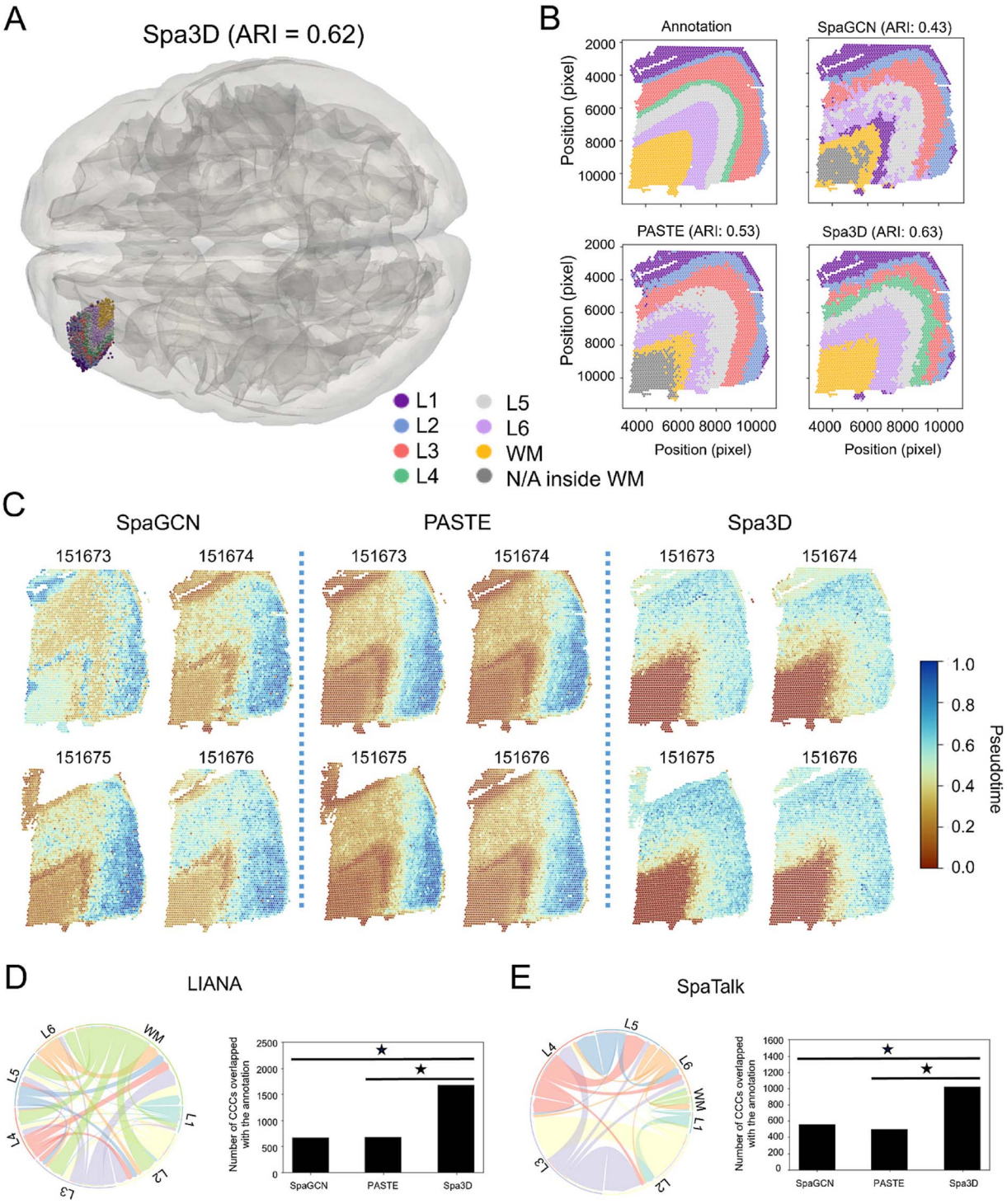

Figure 2 3D characterization of the human dorsolateral prefrontal cortex dataset. (A) Reconstruction of the 3D cellular organization by Spa3D, with incorporation into a human brain structure for descriptive purposes. The IDs of the 2D SRT slices used in this analysis are 151 673, 151 674, 151 675, and 151 676, respectively. The third dimension was based on real spatial coordinates. ARI was calculated based on 3D instead of 2D information. (B) Comparisons of spatial domains among the annotation, SpaGCN, PASTE, and Spa3D. (C) Comparisons on the pseudotime estimated from SpaGCN, PASTE, and Spa3D results. (D and E) cell–cell communication (CCC) analysis based on LIANA (D) and SpaTalk (E). PASTE- and Spa3D-defined clustering results were passed to LIANA and SpaTalk as inputs. The chord diagram (left) illustrated the cell–cell communication frequencies among clusters, while the bar plot (right) showed the number of ligand-receptor pairs overlapped with the annotation. Statistical significances were determined by a two-tailed Fisher exact test. $^{*}P < .05$. The true positive rate (TPR) and false positive rate (FPR) for ligand-receptor pairs (FPLRPs) for panels E and F are shown in Supplementary Fig. 4.

without considering spatial information, such as CellChat [12] and CellPhoneDB [11]. In contrast, SpaTalk is a new algorithm designed for elucidating spatially resolved cell–cell communications using SRT data. We applied both LIANA and SpaTalk to define the cell–cell communication landscape based on spatial clusters identified by the curated annotations from the original study [27], Spa3D, PASTE, and SpaGCN. To assess how well each approach aligned with the curated annotations on cell–cell communications, we calculated the overlapping cell–cell communications between the annotation and each of the three methods examined here (Spa3D, PASTE, and SpaGCN). Specifically, SpaGCN identified 1976 cell–cell communications in total, with 661 overlapping with annotation (Jaccard index = 0.197); PASTE identified 1953 cell–cell communications in total, with 678 overlapping with annotation (Jaccard index = 0.204); Spa3D identified 2075 cell–cell communications in total, with 1679 overlapping with annotation (Jaccard index = 0.689) (Fig. 2D). Interestingly, we found that, based on the LIANA framework, Spa3D identified 1679 ligand-receptor interacting pairs that overlapped with the annotation, which was more than twice the number of overlaps between the annotation and PASTE or SpaGCN (Fig. 2D). A similar trend was observed using the SpaTalk framework (Fig. 2E). SpaGCN identified 2277 cell–cell communications in total, with 558 overlapping with annotation (Jaccard index = 0.164); PASTE identified 1826 cell–cell communications in total, with 501 overlapping with annotation (Jaccard index = 0.167); Spa3D identified 2303 cell–cell communications in total, with 1024 overlapping with annotation (Jaccard index = 0.346). These findings indicate that the 3D spatial construction via the Spa3D algorithm captures the nature of cell–cell communication more accurately than the other methods. Supplementary Fig. 4 provides a false positive rate (FPR) for ligand-receptor pairs and confirms the same trend. These findings demonstrate that Spa3D can identify cell–cell communication networks and providing important insights into the cellular interaction mechanisms underlying spatially resolved biological processes.

Human embryonic heart dataset by barcoded solid-phase RNA capture for spatial transcriptomics profiling platform

To gain a comprehensive understanding of how organs develop and how diseases progress in 3D spatial biology, it is necessary to extract comprehensive 3D knowledge at the organ level [1, 34, 35]. To demonstrate the capability of Spa3D in delineating 3D spatial domains at the whole organ level, we applied it to the human embryonic heart dataset [36] at 6.5 post-conception weeks (PCW) (4 sections) generated by barcoded solid-phase RNA capture for spatial transcriptomics profiling platform [37, 38]. Our findings, as depicted in Fig. 3A, reveal that the 3D cellular organization defined by Spa3D accurately reflects the heart structure as annotated by Asp et al. (2019) [37] (ARI = 0.48 for the 3D spatial structure in Fig. 3A; ARI scores range from 0.44 to 0.57 for each individual slice calculated by Spa3D), thus confirming the capability of Spa3D to accurately capture the spatial organization at the organ level.

To ensure a fair comparison between the 3D cellular organization defined by Spa3D and PASTE-identified "center slice" on spatial domain segmentation, we first showcased a comparison between the PASTE-integrated 2D 'center slice' (ARI = 0.36, Fig. 3B) and the corresponding slice (ARI = 0.57, Fig. 3B) from Spa3D reconstruction. Furthermore, we compared all individual slices reconstructed by Spa3D (ARI from 0.44 to 0.57) (Supplementary Fig. 5) with PASTE's "center slice" and found that Spa3D consistently achieved higher ARI scores than PASTE, not just the one showcased in Fig. 3B. In addition, it is important to note that PASTE failed to show the heart septum between the left and right ventricles, a crucial structural element in the heart (Fig. 3B). In contrast, Spa3D was able to display the septum structure between the left and right ventricles, consistent with our knowledge of heart anatomy and physiology [39–42]. Beyond comparison with the PASTE integration, we also evaluated Spa3D against two other methods, STAGATE and GraphST. Supplementary Fig. 6 demonstrates that Spa3D attained a higher ARI.

To explore domain-specific differentially expressed genes, we applied edgeR and Seurat packages on differential expression analysis to detect sdaSVGs based on Spa3D- and PASTE-defined spatial domains. As shown in Supplementary Fig. 7, in most of the spatial domains, the sdaSVGs detected by Spa3D showed higher overlap with known heart-specific gene set than the ones defined by PASTE, confirming that Spa3D-defined sdaSVGs align better with known biological knowledge.

We next assessed the ability of Spa3D to elucidate the organ-level tempo-spatial development patterns. We aimed to comprehend the spatial and temporal developmental dynamics of the human embryonic heart. To achieve this, we compared Spa3D-defined 3D reconstructions at 6.5 post-conception weeks (PCW) (four sections with IDs from 9 to 12) and 9 PCW (2 sections with IDs from 16 to 17). Figure 3C illustrates the Spa3D-defined spatial domain dynamics from 6.5 to 9 PCW. We observed significant changes in spatial domains during the heart development process, including the increase in the size of the spatial domain representing vessels and outflow tracts (green color) and the spatial domain for the compact ventricular myocardium and septum (red color). These findings are in line with current knowledge of human heart anatomy and physiology from 6.5 to 9 PCW [39, 42–44].

To continue the investigation of the temporal dynamics of organ-level development patterns, we performed the pseudotime inference analysis by DPT method [21] at 6.5 and 9 PCW to infer the pseudo-spatial trajectories at these two time points based on Spa3D results (Fig. 3D). Interestingly, while two distinct spatial domains (red and blue in Fig. 3C) were observed in the ventricular myocardium, these two domains were indistinguishable with similar pseudotime scores in Fig. 3D. We resolved this seeming contradiction through a deep exploration of the available anatomy and physiology evidence. Specifically, both spatial locations and molecular makers of these two domains in Fig. 3C (e.g. IGFBP3, LDHA, PGK1, and ENO1 for red domain, and MYL2, MYH7, FHL2, and PLN for blue domain) aligned well with known compact (red) and trabecular (blue) ventricular myocardium structures in human hearts [36, 45–47]. This result confirms that the Spa3D-defined spatial domains in Fig. 3C are consistent with known cell types. In contrast, Fig. 3D indicates that these two distinct cell types share similar pseudotime scores and temporal trajectory patterns. These results agree with experimental evidence that the formation and specification of compact and trabecular ventricular myocardium both occur during the same time period (weeks 5–8) of human embryonic life, as part of normal cardiac morphogenesis [45–49]. Collectively, these results support that 3D reconstruction via Spa3D can assist the spatial segmentation and pseudotime inference analysis to achieve good agreement with existing knowledge.

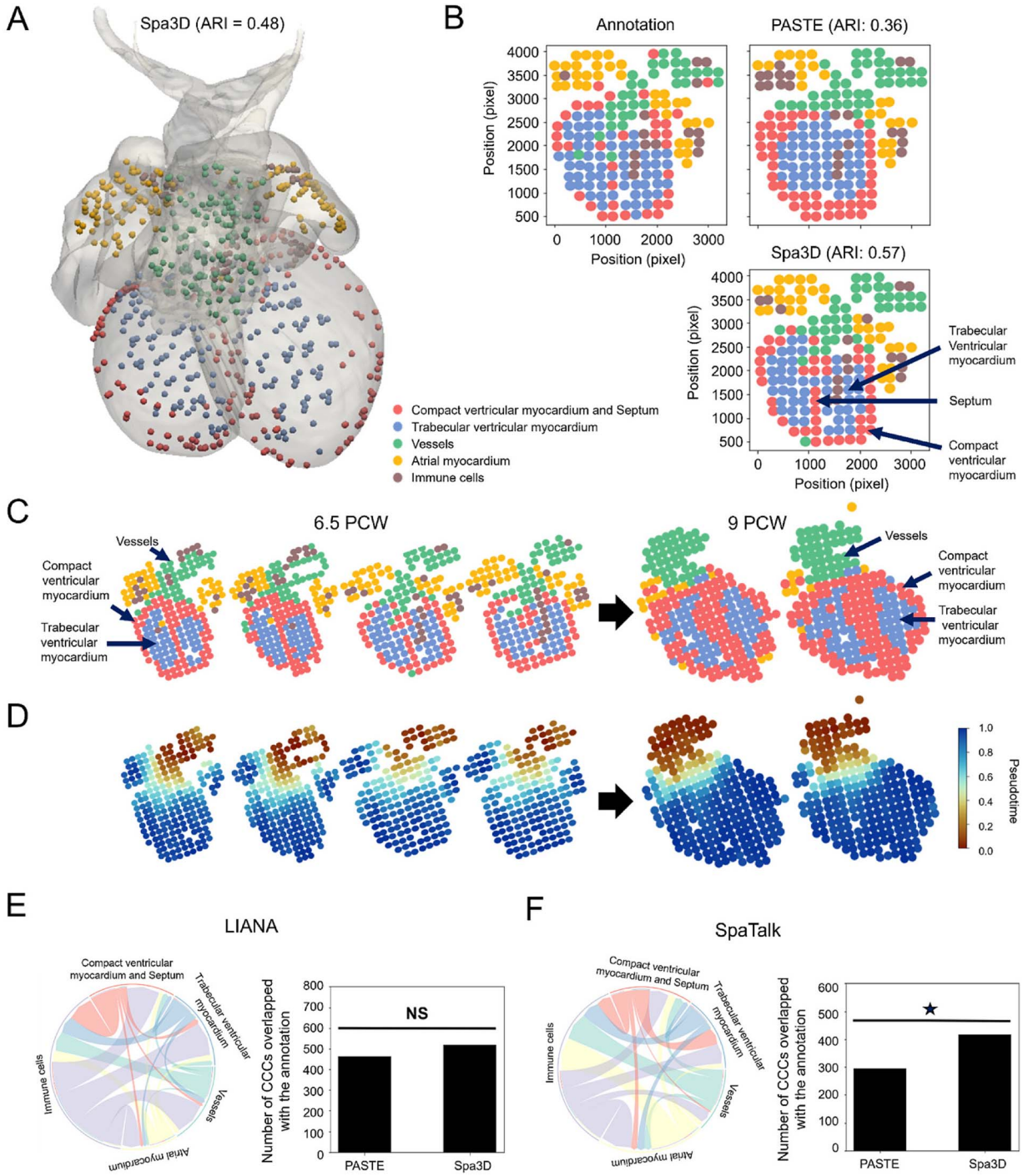

Figure 3 3D characterization of tempo-spatial development patterns in the human embryonic heart dataset. (A) Reconstruction of the 3D cellular organization by Spa3D, with incorporation into a human heart structure for descriptive purposes. The IDs of the four slices are 9, 10, 11, and 12, respectively. (B) Comparisons of spatial domains among the annotation, PASTE, and Spa3D. (C) Spa3D reconstructed cellular organization from 6.5 PCW to 9 PCW. (D) Spa3D-defined organ-level tempo-spatial development patterns from 6.5 PCW to 9 PCW. The six slices at 6.5 PCW and 9 PCW are processed together to present a consistent pseudotime. (E and F) cell–cell communication (CCC) analysis based on LIANA (E) and SpaTalk (F). PASTE- and Spa3D-defined clustering results were passed to LIANA and SpaTalk as inputs. The chord diagram (left) illustrated the cell–cell communication frequencies among clusters, while the bar plot (right) showed the number of ligand-receptor pairs overlapped with the annotation from single-cell mapping. Statistical significances were determined by a two-tailed Fisher exact test. NS for non-significant. $^{*}P < .05$. The true positive rate (TPR) and false positive rate (FPR) for ligand-receptor pairs (FPLRPs) for panels E and F are shown in Supplementary Fig. 8.

Finally, we investigated the capability of Spa3D to accurately identify ligand-receptor signaling pathways involved in cell–cell communication in comparison with PASTE. To evaluate their performance, we calculated the percentage of overlapping ligand-receptor pairs between the annotated from Asp et al. (2019) [37] and Spa3D or PASTE results (Fig. 3E and F). Under LIANA framework (Fig. 3E), PASTE identified 702 cell–cell communications in total, with 464 overlapping with annotation (Jaccard index = 0.437); Spa3D identified 771 cell–cell communications in total, with 519 overlapping with annotation (Jaccard index = 0.483). Under SpaTalk framework (Fig. 3F), PASTE identified 674 cell–cell communications in total, with 295 overlapping with annotation (Jaccard index = 0.209); Spa3D identified 800 cell–cell communications in total, with 415 overlapping with annotation (Jaccard index = 0.293). Therefore, under both LIANA and SpaTalk framework, Spa3D identified more ligand-receptor interacting pairs that overlapped with the annotation than PASTE. A statistically significant difference was observed under the SpaTalk framework (Fig. 3F), while LIANA showed the same trend but was not statistically significant. LIANA's lack of spatial information likely explains its non-significant results and lower accuracy versus SpaTalk for spatial transcriptomics. Supplementary Fig. 8 shows false-positive rates (FPRs) for ligand-receptor pairs, confirming this trend. Thus, Spa3D effectively enhances cell–cell communication analysis via 3D reconstruction.

High resolution developing *Drosophila* embryos dataset by stereo-seq platform

To assess the performance of Spa3D on high-resolution spatial transcriptomic data, we analyzed a dataset [50] derived from developing *Drosophila* embryos using Stereo-seq, which captured the expression of 13,668 genes at near-single-cell resolution. The dataset includes 16 consecutive slices sampled at uniform intervals covering the entire embryo during stage E14–16 (Fig. 4A). For 3D reconstruction, we selected four representative slices (slices 9–12). Spa3D well reconstructed the 3D architecture of these slices (Fig. 4B, ARI = 0.29). Using slice 11 as the center slice, we found that Spa3D (ARI = 0.38) outperformed PASTE (ARI = 0.27) in domain segmentation (Figs 4C–E). In particular, Spa3D more accurately identified tracheal and CNS cells compared with PASTE (Fig. 4D and E).

3D spatial trajectory in the mouse hypothalamus dataset by MERFISH platform

To demonstrate the versatility of Spa3D in analyzing SRT data from various platforms, we studied a dataset [3] from the mouse hypothalamic preoptic region generated using the multiplexed error-robust fluorescence *in situ* hybridization (MERFISH) approach. This dataset is distinct from the 10x Genomics Visium, ST and Stereo-Seq platforms presented in Figs 2–4, respectively, and represents an imaging-based singe-cell resolution SRT approach.

First, we conducted a comparative analysis of Spa3D and PASTE on this mouse hypothalamus dataset to assess their ability to accurately identify spatial domains. Our results showed that Spa3D not only accurately reflected the anatomical structure of the hypothalamus as annotated by Moffitt et al. (2018) [3] (ARI = 0.50 for the whole 3D reconstruction, ranging from 0.49 to 0.53 for each individual SRT slice calculated by Spa3D, Fig. 5A, with a planar layout in Supplementary Fig. 9), but also outperformed PASTE-defined central slice in clustering accuracy (ARI = 0.04, Supplementary Fig. 10).

To further examine the biological significance of Spa3D- and PASTE-defined spatial domains, we queried sdaSVGs for each annotated hypothalamus domain defined by Spa3D and PASTE with a known hypothalamus gene set defined by the Allen Mouse Brain Atlas [30]. As shown in Supplementary Fig. 11, in most of these spatial domains, we observed that Spa3D-defined sdaSVGs showed higher overlap with known hypothalamus gene set than sdaSVGs defined by PASTE, by both edgeR (Supplementary Fig. 11A) and Seurat algorithms (Supplementary Fig. 11B). Moreover, several sdaSVGs defined by Spa3D but missed by PASTE (e.g. IGF1R [51, 52], ESR1 [53–55], PNOC [56], and OXT [57, 58]) have experimental evidence for hypothalamic function, validating Spa3D's ability to detect histology-associated, domain-specific genes.

Second, one major advantage of Spa3D is the ability to uncover spatial trajectories in a 3D manner, which refers to the trajectory analysis that arranges cells based on their spatial patterns. This is achieved by aligning all cells across 2D SRT slices to reconstruct the intact 3D cellular organization (Fig. 5A, left panel), which enables the visualization of 3D spatial trajectories of various cell types (Fig. 5A, right panel). Conversely, stacking 2D slices in an arbitrary way without precise 3D alignment of all cells can result in inaccurate cell location determination, making it difficult to detect 3D spatial trajectories of different cell types. To compare the 3D spatial trajectory patterns revealed by Spa3D and PASTE in this hypothalamus dataset, we focused on two popular neuron types in the hypothalamic preoptic region: mature oligodendrocytes (OD mature) (green) and excitatory neurons (blue), to avoid too many cell types in one figure to mask the trajectory patterns (Fig. 5B). We found that Spa3D and PASTE revealed similar patterns for MO cells after 3D spatial alignment and reconstruction (green, Fig. 5B). However, for excitatory neurons, especially in the anterior hypothalamus, these two algorithms uncovered distinct patterns (Figs 5B–E): PASTE detected few excitatory neurons anteriorly and a punctuated posterior increase, whereas Spa3D identified more abundant and gradually increasing anterior excitatory neurons (Fig. 5C). An independent EASI-FISH study [59] confirmed the abundance and a gradually increasing gradient of excitatory neurons in hypothalamus, consistent with the findings by Spa3D. In addition, Spa3D better reveals the trajectory of spatial position change of excitatory neurons from anterior to posterior, as demonstrated in the linear regression results of vertical cell positions within slices against the anatomical positions across the slices from anterior to posterior (Fig. 5D and E).

Discussion

Spa3D enables comprehensive 3D-based spatial segmentation analysis by incorporating spatial distances both across and within slices during 3D graph construction and GCN training. This framework naturally extends to 3D pseudotime inference and 3D cell–cell communication analysis (Fig. 2 and 3). In addition, Spa3D supports 3D reconstruction from slices containing distinct cell types and heterogeneous gene expression patterns (Fig. 5), demonstrating its applicability to complex biological tissues such as the brain and tumors. We further evaluated the performance of Spa3D on spatial transcriptomics (SRT) datasets generated by four major platforms, 10x Genomics Visium, ST, Stereo-seq, and MERFISH, which span a wide range of spatial resolutions. Spa3D can be readily applied to other emerging SRT technologies such as seqFISH+, STARmap, and Slice-seq, underscoring its versatility for diverse spatially resolved omics applications.

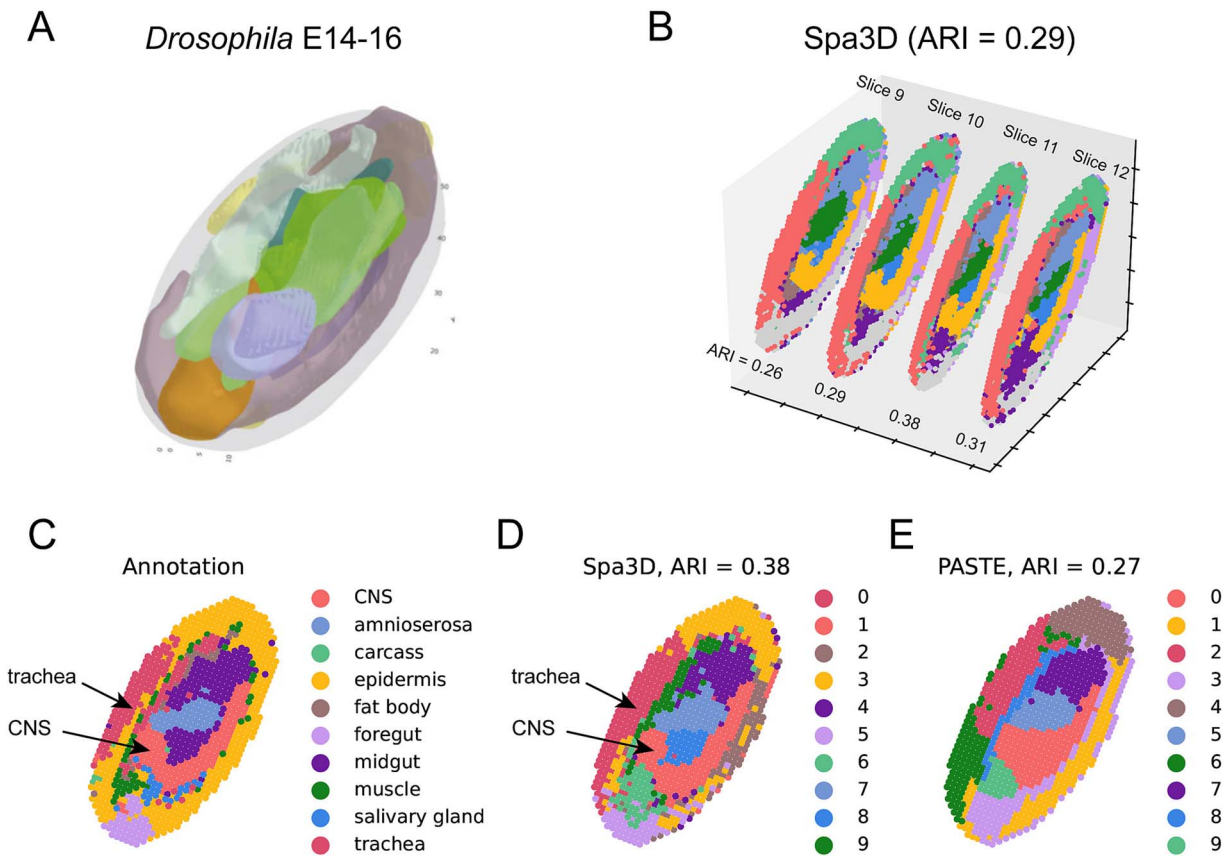

Figure 4 3D characterization of developing Drosophila embryos dataset. (A) The schematic of 3D Drosophila embryos structure at stage E14–16. (B) Reconstruction of the 3D structure of slices 9–12 by Spa3D. (C) Annotation of cells in slice 11. (D) Doman segmentation of slice 11 by Spa3D. (E) Doman segmentation of slice 11 by generating center slice with PASTE.

While Spa3D provides an effective framework for integrating multi-slice SRT data, its performance is partially influenced by the accuracy of inter-slice alignment. In this study, we either used the pre-aligned coordinates provided in the original publication (Fig. 4) or applied the alignment methods implemented in PASTE (Figs 2, 3, and 5). Although techniques of 3D alignment across heterogeneous tissue sections have advanced, most existing approaches primarily rely on molecular features and often overlook complementary information contained in histological images. We envision that incorporating histological features alongside enhanced molecular signals will further improve 3D alignment fidelity. The improved version of Spa3D in our follow-up study will leverage cellular components, morphological features, and tissue architecture to guide alignment, ensuring cross-slice consistency and preserving local tissue integrity. This improvement will enable more accurate 3D reconstructions and provide deeper biological insights.

Beyond spatial transcriptomics, Spa3D offers a foundation for extending 3D reconstruction to other spatial omics modalities, including spatial epigenomics (e.g. spatial ATAC-seq and spatial-CUT&Tag) and spatial proteomics. Such extensions would enable exploration of epigenomic regulation and protein interaction networks within true 3D tissue contexts. By restoring tissue morphology and embedding spatial coordinates into multi-omics data, Spa3D establishes a general framework for advancing our understanding of cellular function, tissue development, and disease progression in 3D space.

Methods

Spatial pattern enhancement

We have used two approaches below to enhance the spatial pattern. First, we have transformed the gene expression from the real-number domain to the complex-number domain. We first calculated the analytic expression from the real-number expression:

$$s_a = s(x) + j\hat{s}(x). \tag{1}$$

Here, the s is the gene expression at spatial point $\mathbf{x}$, $\hat{s}$ is the Hilbert transform of s. s_a is the analytic signal. We then calculated the envelop s_e of the gene expression from the analytic signal:

$$s_e = |s_a|\,. \tag{2}$$

Considering the gene expression is the oscillating signal, the envelope of the signal consists of its local extreme values. It generalizes the local gene expression values into instantaneous gene expression.

This SPE approach works effectively for the DLPFC dataset (Fig. 2), in which the SRT samples are sufficient, and the spatial structures are well organized. However, the human embryonic heart dataset (Fig. 3) contains fewer SRT samples, and the mouse hypothalamus dataset (Fig. 4) provide single-cell resolution. To control the degree of

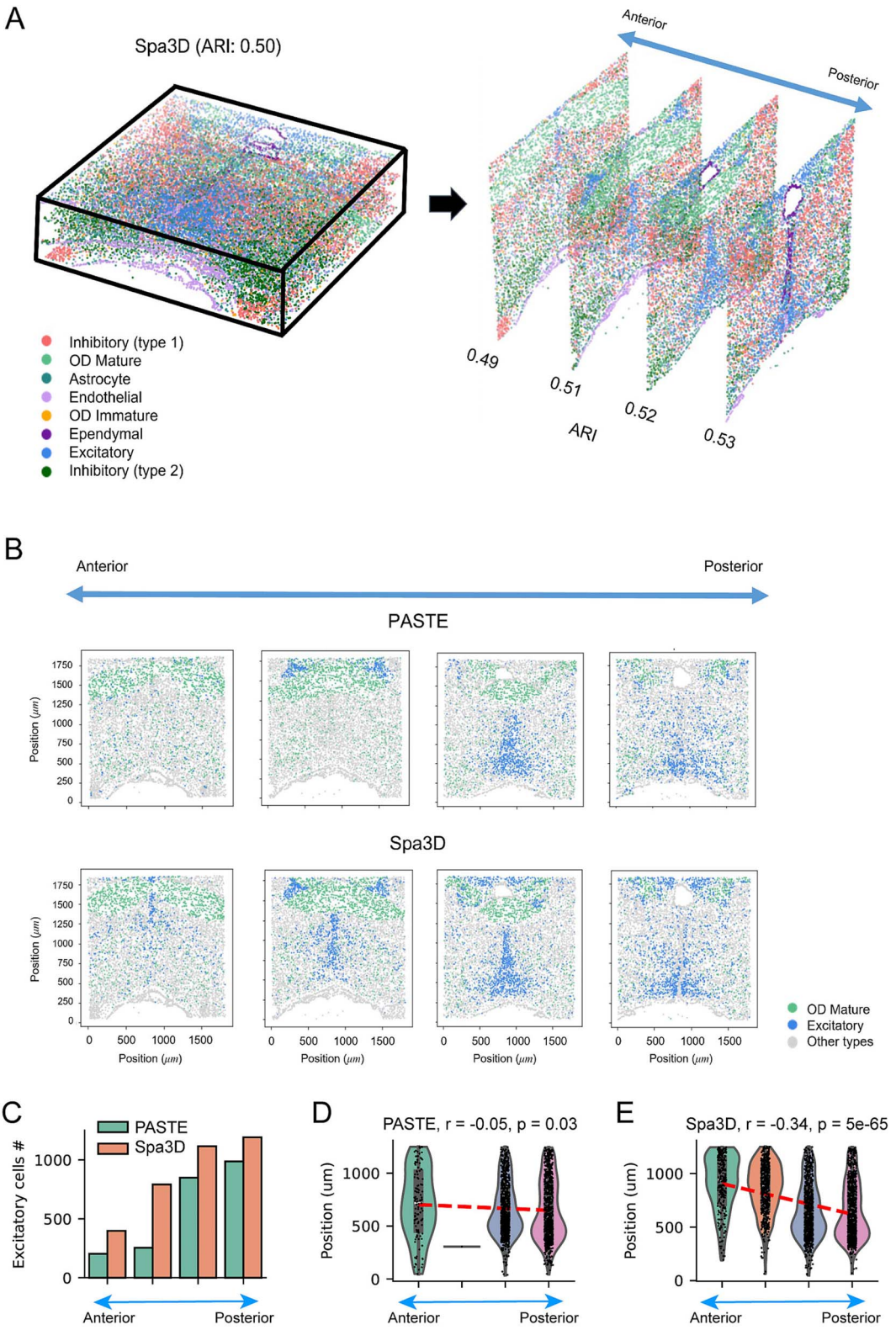

Figure 5 3D spatial trajectory in the mouse hypothalamus dataset based on the MERFISH platform. (A) The left panel displays the reconstruction of the 3D cellular organization by Spa3D. The distance between adjacent slices is 50 μm. For descriptive display purposes, we use different display scales for the z-axis and horizontal dimensions. The right panel presents the spatial trajectory from anterior to posterior. A planar layout of the Spa3D result is shown in Supplementary Fig. 9. (B) Comparison of PASTE and Spa3D in presenting the spatial trajectory of OD mature and excitatory cells from anterior to posterior. (C) The total number of excitatory cells across the four slices in PASTE (green) and Spa3D (orange) representations. (D and E) The position distributions of excitatory cells in the lower half of the image across the four slices in PASTE (D) and Spa3D (E) representations. Only excitatory cells in the lower half were counted to display the trajectory because the cells in the upper half may belong to a separate group. There is no excitatory cell in the lower half of the second slice in PASTE representation. The red lines display the linear regression of vertical cell positions within the slices against the anatomical positions across slices from anterior to posterior.

enhancement under such varying conditions, we developed a second SPE approach that applies the anti-leakage Fourier transform (ALFT) to extract the dominant components of spatial patterns. The ALFT was proposed by Xu et al. (2005, 2010) [60, 61] for seismic data regularization. It was later used by Tang and McMechan (2017) [62] to extract the normal direction of reflection image in local windows.

In a local spatial window, we use the forward Fourier transform to project the real-domain signal, i.e. the gene expression $s(x)$, into the wavenumber domain:

$$\overline{S}(k) = \int_{-\infty}^{\infty} s(x) e^{-ikx} dx, \tag{3}$$

where $\overline{S}(k)$ denotes the complex Fourier coefficient of the gene expression $s(x)$at wavenumber k.If a signal has spatial structure, its energy tends to concentrates at specific wavenumbers. In contrast, spatially unstructured signals (e.g. random noise or point sources) exhibit energy dispersed across a wide range of wavenumbers. This property underlies the ALFT algorithm's ability to isolate meaningful spatial patterns.

ALFT works by iteratively extracting the highest-energy component in the Fourier domain until the residual signals in the real domain fall below a set threshold:

$$\xi_i = \xi_{i-1} - s^f_{i,\max}(x), \tag{4}$$

where ξ_i and ξ_{i-1} are the residual signals at the current iterations i and $i-1$, respectively. The initial residual is defined as:

$$\xi_0 = s(x). \tag{5}$$

Here, $s^f_{i,\max}(x)$ is the inverse Fourier transform of the dominant frequency component $\overline{S}_{i,\max}(k)$:

$$s^f_{i,\max}(x) = \int_{-\infty}^{\infty} \overline{S}_{i,\max}(k) e^{ikx} dk, \tag{6}$$

where $\overline{S}_{i,\max}(k)$ is the complex Fourier coefficient at the wavenumber $k$with the largest magnitude at iteration i, corresponding to the dominant spatial frequency component extracted at that step. By successively extracting these high-energy components and updating the residual, ALFT progressively emphasizes coherent spatial structures while suppressing unstructured background noise.

Equations 4 to 6 perform well when spatial patterns are strong, and wavenumber values are sparse. However, gene expression patterns are typically weaker and less sparse than seismic signals, making the iterative inverse Fourier transform computationally expensive. To improve efficiency, we perform the iteration in the wavenumber domain:

$$\zeta_i = \zeta_{i-1} - \left|\overline{S}_{i,\max}(k)\right|, \tag{7}$$

where ζ_i, is the residual energy in the wavenumber domain at iteration i and

$$\zeta_0 = \int \left|\overline{S}(k)\right| dk. \tag{8}$$

This approach avoids repeated inverse transforms while maintaining the same iterative filtering principle. We could optionally square the $\left|\overline{S}(k)\right|$ terms in equations 7 to 8, but this is not necessary since the iteration already achieves effective filtering of dominant wavenumbers.

After identifying all effective wavenumber points, we perform a single inverse Fourier transform to map them back to the spatial domain, avoiding repeated transforms during each iteration. This is an efficient way for the gene expression as the value in the wavenumber domain is often not sparse. If the energy threshold $\zeta_{threshold}$ is small (e.g. 5% of the total energy), the iteration can alternatively accumulate the lowest energy components:

$$\varsigma_i = \varsigma_{i-1} + \left|\overline{S}_{i,\min}(k)\right|, \tag{9}$$

with

$$\varsigma_0 = 0. \tag{10}$$

This alternative follows the same principle as ζ_i, but in reverse, and provides flexibility for controlling the retained energy. One can also rank all wavenumber magnitudes before iteration and select the top or bottom entries at each step.

Overall, the ALFT-based spatial pattern enhancement iteratively identifies and extracts the dominant spatial frequency components in the wavenumber domain. Each wavenumber $k$corresponds to a particular spatial variation in the real domain, and by combining these components, the method reconstructs the prominent spatial patterns. By suppressing lower-energy components, which typically represent noise, the process enhances the primary spatial structures while simultaneously performing denoising.

To empirically validate the assumption that spatial signals concentrate energy at specific wavenumbers, we computed the fraction of Fourier power in the top 5% of wavenumbers (Top5PercentEnergy) across all genes in four spatial omics datasets from the heart. We observed that a substantial portion of genes (47.09%–49.70% across datasets) have Top5PercentEnergy exceeding 0.9, with maximum values reaching 0.999, while many other genes exhibit moderately concentrated energy. These results indicate that nearly half of the genes carries highly concentrated spatial signals, whereas others are more evenly distributed, consistent with the expected diversity of spatial structures across genes. Overall, this analysis provides quantitative support for the principles underlying ALFT- and Hilbert transform-based spatial pattern enhancement in our pipeline.

3D reconstruction based on graph convolutional network

For 3D reconstruction, as each slice may have inter-slice registration errors, we first applied pairwise alignment implemented in PASTE [24] to the multiple 2D SRT slices before assembling the 3D dataset. The 3D data can be used for both 3D reconstruction and pseudotime inference analysis (e.g. Fig. 2A and 2C). We then utilized the full 3D spatial information, including the depth z coordinate, to calculate the adjacency matrix A for graph construction. When 3D histology images are involved in calculating the Euclidean distance, Spa3D provides an option to apply a penalty parameter σ to the depth z coordinate to correct for anisotropic resolution across dimensions:

$$D_{j,k} = \sqrt{(x_j - x_k)^2 + (y_j - y_k)^2 + (\sigma z_j - \sigma z_k)^2 + (I_j - I_k)^2}. \tag{11}$$

where the j and k denote two spots, (x, y, z) is the 3D coordinate of a spot, and the I is a distance measured by the RGB value of the histology image in a local window. In typical spatial transcriptomics data, the z-axis (across slices) is sampled more coarsely than the x-y plane, leading to lower effective resolution along depth. To compensate, we scale the z values using $\sigma = (l_c + d)/l_c$, where l_c is the center-to-center distance between adjacent spots within a single slice (100 μm) and d is the spot diameter (55 μm) in the 10x Genomics Visium platform, giving $\sigma = 1.55$. This scaling increases the contribution of z-axis differences to the Euclidean distance, correcting for lower axial resolution. If isotropic resolution is assumed ($\sigma = 1$), Equation 11 reduces to the standard 3D Euclidean distance:

$$D_{j,k} = \sqrt{(x_j - x_k)^2 + (y_j - y_k)^2 + (z_j - z_k)^2}. \tag{12}$$

The $D_{j,k}$ will be used to construct the adjacent matrix A which consists of A_{ij}:

$$A_{ij} = e^{\left(-\frac{D_{ij}^2}{2\ell^2}\right)}, \tag{13}$$

where A_{ij} is the edge weight between nodes i and j, and ℓ is a parameter that determines the scale of the kernel, affecting how quickly the values decay with increasing distance. We used Louvain for the initialization of clustering analysis and used GCN to iteratively update the 3D reconstruction by optimizing the loss function. The graph convolution is

$$H = \varphi(AXW + b) \tag{14}$$

where A is the adjacent matrix calculated using full 3D coordinates (referring to equations 11 and 12), X is the matrix of the input features, W is the weight matrix of the layer, b is the bias vector, $\varphi(\bullet)$ denotes the nonlinear activation, and H is the output. The loss function uses Kullback–Leibler (KL) divergence:

$$KL(p \| q) = \sum_i \sum_j p_{ij} \log \frac{p_{ij}}{q_{ij}}. \tag{15}$$

Here, q is the predicted soft assignment distribution, representing how likely each embedded data point is to belong to a given cluster. Mathematically, q is calculated using a Student's t-distribution with one degree of freedom (also known as the Cauchy distribution) as a kernel to measure the similarity between the i-th embedded data point z_i and the j-th cluster center μ_j:

$$q_{ij} = \frac{\left(1 + \|z_i - \mu_j\|^2\right)^{-1}}{\sum_{j'} \left(1 + \|z_i - \mu_{j'}\|^2\right)^{-1}}. \tag{16}$$

In equation 15, p is the target distribution, used to guide the optimization of the clustering by serving as a reference or "target" for updating the model's parameters. The target distribution is calculated in a way that emphasizes data points with high confidence in their cluster assignment and minimizes the entropy of the distribution. p can be calculated from q:

$$p_{ij} = \frac{q_{ij}^2 / \sum_{i'} q_{i'j}}{\sum_{j'} \left(q_{ij'}^2 / \sum_{i'} q_{i'j'} \right)}. \tag{17}$$

The Kullback–Leibler divergence between q and p is often minimized during training.

Equation 14 is a standard GCN layer formulation [63], and equations 15 to 16 represent the routine process for implementing unsupervised deep embedding for clustering analysis [64]. The approach is used by Hu et al. [8]. The main difference in our approach is that we use 3D coordinates to calculate the adjacency matrix for the graph, which is then used in the subsequent calculations.

DLPFC dataset

We selected the first approach, instantaneous amplitude, to enhance the spatial pattern due to the large sample size. To be consistent with the PASTE method [24], we used the original data provided from the PASTE GitHub page to generate the PASTE-defined 'center slice' in Fig. 2B.

Human heart dataset

The annotation was obtained from Asp et al. (2019) [37] by merging similar, smaller clusters into five larger ones. As the PASTE paper does not provide the 'center slice' result for this example, we used the PASTE scripts from its GitHub page to generate the integrated 'center slice' displayed in Fig. 3B. We applied a SpaceFlow-based DPT [65] for the pseudotime inference analysis in Fig. 3E, using 3D spatial coordinates and time information.

Drosophila embryos dataset

The annotation was obtained from the original paper [50]. We selected the slices 9–11 in E14–16 stage for analysis. The dataset contains both raw pixels and pre-aligned positions. For Spa3D analysis, we used the raw pixels to do spatial enhancement and the pre-aligned positions to do domain segmentation. For PASTE analysis, we used PASTE-aligned positions to do domain segmentation.

Hypothalamic preoptic region dataset

Because the dataset provided by the MERFISH technology is at the single-cell level, we used the second approach, revised ALFT in local windows, to enhance the local spatial pattern.

Downstream analysis of Spa3D and PASTE results

We calculated pseudotime by running the diffusion pseudotime (DPT) method [21] using the Spa3D and PASTE embedding, respectively. For cell–cell communication analysis, we used two distinct frameworks, LIANA [33] and SpaTalk [14], for independent analysis. To define domain-specific SVGs, we performed differential expression (DE) analysis using spots from a target domain versus all other domains. To achieve a robust list of SVGs, we applied edgeR [28] and Seurat [29] packages, both of which are state-of-art DE analysis methods.

Key Points

- Most existing spatial omics analysis methods rely on 2D data, limiting their ability to capture full spatial and developmental tissue complexity
- Spa3D incorporates physical z-axis distances, enabling accurate 3D modeling even when adjacent slices vary in tissue structure and composition
- Spa3D reconstructs true 3D spatial structures from 2D SRT slices using graph convolutional networks and anti-leakage Fourier transforms
- Spa3D enhances spatial domain detection, revealing detailed cell–cell communication and organ-level development patterns across multiple spatial omics platforms
- Spa3D enables novel biological discoveries by revealing spatial features and trajectories not detectable using traditional 2D transcriptomic analysis approaches

Acknowledgements

The resources of the high-performance computing environment from the Quantitative Biomedical Research Center (QBRC) and BioHPC at UT Southwestern Medical Center, as well as the Texas Advanced Computing Center (TACC) at The University of Texas at Austin, are gratefully acknowledged. We also thank Ms. Jessie Norris for proofreading this manuscript.

Author contributions

CT, YZ, XX, and LX conceived and designed the study. CT, YZ, and XX developed the Spa3D algorithm, generated the scripts and GitHub page, and performed the data analysis. LD and LY were involved in the data analysis. LX and GX acquired the funding. CT, YZ, XX, QL, GX, and LX wrote and revised the manuscript. All authors have read, revised, and approved the final manuscript.

Supplementary data

Supplementary data is available at *Briefings in Bioinformatics* online.

Conflict of interest

All the authors declare that they have no competing interests.

Funding

This work was supported by the following funding: the Rally Foundation, Children's Cancer Fund (Dallas), the Cancer Prevention and Research Institute of Texas (RP180319, RP200103, RP220032, RP170152 and RP180805), and the National Institutes of Health funds (R01DK127037, R01CA263079, R21CA259771, P30CA142543, UM1HG011996, and R01HL144969), and the support to the Data Science Shared Resource from Cancer Center Support Grant P30 CA142543 (to L.X.); the National Institutes of Health (1R01GM115473, 1R01GM140012, 5R01CA152301, P30CA142543, P50CA70907, R35GM136375); and the Cancer Prevention and Research Institute of Texas (RP180805, RP190107) (to G. X.).

Data availability

The datasets used in this study are publicly available, and the original publications for each dataset are cited in the Methods section. The source code for Spa3D can be downloaded from GitHub (https://github.com/Lin-Xu-lab/Spa3D.git).

Code availability

The Spa3D package is available at https://github.com/Lin-Xu-lab/Spa3D.git.

References

1. Moses L, Pachter L. Museum of spatial transcriptomics. *Nat Methods* 2022;**19**:534–46. https://doi.org/10.1038/s41592-022-01409-2
2. Rao A, Barkley D, Franca GS *et al.* Exploring tissue architecture using spatial transcriptomics. *Nature* 2021;**596**:211–20. https://doi.org/10.1038/s41586-021-03634-9
3. Moffitt JR, Bambah-Mukku D, Eichhorn SW *et al.* Molecular, spatial, and functional single-cell profiling of the hypothalamic preoptic region. *Science* 2018;**362**:eaau5324. https://doi.org/10.1126/science.aau5324
4. Rodriques SG, Stickels RR, Goeva A *et al.* Slide-seq: a scalable technology for measuring genome-wide expression at high spatial resolution. *Science* 2019;**363**:1463–7. https://doi.org/10.1126/science.aaw1219
5. Shah S, Takei Y, Zhou W *et al.* Dynamics and spatial genomics of the nascent transcriptome by intron seqFISH. *Cell* 2018;**174**:363–376.e16. https://doi.org/10.1016/j.cell.2018.05.035
6. Vickovic S, Eraslan G, Salmén F *et al.* High-definition spatial transcriptomics for in situ tissue profiling. *Nat Methods* 2019;**16**:987–90. https://doi.org/10.1038/s41592-019-0548-y
7. Wang X, Allen WE, Wright MA *et al.* Three-dimensional intact-tissue sequencing of single-cell transcriptional states. *Science* 2018;**361**:eaat5691. https://doi.org/10.1126/science.aat5691
8. Hu J, Li X, Coleman K *et al.* SpaGCN: integrating gene expression, spatial location and histology to identify spatial domains and spatially variable genes by graph convolutional network. *Nat Methods* 2021;**18**:1342–51. https://doi.org/10.1038/s41592-021-01255-8
9. Zhao E, Stone MR, Ren X *et al.* Spatial transcriptomics at subspot resolution with BayesSpace. *Nat Biotechnol* 2021;**39**:1375–84. https://doi.org/10.1038/s41587-021-00935-2
10. Long Y, Ang KS, Li M *et al.* Spatially informed clustering, integration, and deconvolution of spatial transcriptomics with GraphST. *Nat Commun* 2023;**14**:1155. https://doi.org/10.1038/s41467-023-36796-3
11. Efremova M, Vento-Tormo M, Teichmann SA *et al.* CellPhoneDB: inferring cell-cell communication from combined expression of multi-subunit ligand-receptor complexes. *Nat Protoc* 2020;**15**:1484–506. https://doi.org/10.1038/s41596-020-0292-x
12. Jin S, Guerrero-Juarez CF, Zhang L *et al.* Inference and analysis of cell-cell communication using CellChat. *Nat Commun* 2021;**12**:1088. https://doi.org/10.1038/s41467-021-21246-9
13. Browaeys R, Saelens W, Saeys Y. NicheNet: Modeling intercellular communication by linking ligands to target genes. *Nat Methods* 2020;**17**:159–62. https://doi.org/10.1038/s41592-019-0667-5
14. Shao X, Li C, Yang H *et al.* Knowledge-graph-based cell-cell communication inference for spatially resolved transcriptomic data with

SpaTalk. *Nat Commun* 2022;**13**:4429. https://doi.org/10.1038/s41467-022-32111-8
15. Cang Z, Zhao Y, Almet AA *et al.* Screening cell-cell communication in spatial transcriptomics via collective optimal transport. *Nat Methods* 2023;**20**:218–28. https://doi.org/10.1038/s41592-022-01728-4
16. Fischer DS, Schaar AC, Theis FJ. Modeling intercellular communication in tissues using spatial graphs of cells. *Nat Biotechnol* 2023;**41**:332–6. https://doi.org/10.1038/s41587-022-01467-z
17. Pham D, Tan X, Xu J *et al.* Robust mapping of spatiotemporal trajectories and cell–cell interactions in healthy and diseased tissues. *Nat Commun*. 2023;**14**:7739.
18. Qiu X, Mao Q, Tang Y *et al.* Reversed graph embedding resolves complex single-cell trajectories. *Nat Methods* 2017;**14**:979–82. https://doi.org/10.1038/nmeth.4402
19. Cao J, Spielmann M, Qiu X *et al.* The single-cell transcriptional landscape of mammalian organogenesis. *Nature* 2019;**566**:496–502. https://doi.org/10.1038/s41586-019-0969-x
20. Wolf FA, Hamey FK, Plass M *et al.* PAGA: graph abstraction reconciles clustering with trajectory inference through a topology preserving map of single cells. *Genome Biol* 2019;**20**:59. https://doi.org/10.1186/s13059-019-1663-x
21. Haghverdi L, Buttner M, Wolf FA *et al.* Diffusion pseudotime robustly reconstructs lineage branching. *Nat Methods* 2016;**13**:845–8. https://doi.org/10.1038/nmeth.3971
22. Street K, Risso D, Fletcher RB *et al.* Slingshot: cell lineage and pseudotime inference for single-cell transcriptomics. *BMC Genomics* 2018;**19**:477. https://doi.org/10.1186/s12864-018-4772-0
23. He Y, Tang X, Huang J *et al.* ClusterMap for multi-scale clustering analysis of spatial gene expression. *Nat Commun* 2021;**12**:5909. https://doi.org/10.1038/s41467-021-26044-x
24. Zeira R, Land M, Strzalkowski A *et al.* Alignment and integration of spatial transcriptomics data. *Nat Methods* 2022;**19**:567–75. https://doi.org/10.1038/s41592-022-01459-6
25. Xu C, Jin X, Wei S *et al.* DeepST: identifying spatial domains in spatial transcriptomics by deep learning. *Nucleic Acids Res* 2022;**50**:e131. https://doi.org/10.1093/nar/gkac901
26. Li Z, Zhou X. BASS: multi-scale and multi-sample analysis enables accurate cell type clustering and spatial domain detection in spatial transcriptomic studies. *Genome Biol* 2022;**23**:168. https://doi.org/10.1186/s13059-022-02734-7
27. Maynard KR, Collado-Torres L, Weber LM *et al.* Transcriptome-scale spatial gene expression in the human dorsolateral prefrontal cortex. *Nat Neurosci* 2021;**24**:425–36. https://doi.org/10.1038/s41593-020-00787-0
28. Robinson MD, McCarthy DJ, Smyth GK. edgeR: a Bioconductor package for differential expression analysis of digital gene expression data. *Bioinformatics* 2010;**26**:139–40. https://doi.org/10.1093/bioinformatics/btp616
29. Butler A, Hoffman P, Smibert P *et al.* Integrating single-cell transcriptomic data across different conditions, technologies, and species. *Nat Biotechnol* 2018;**36**:411–20. https://doi.org/10.1038/nbt.4096
30. Sunkin SM, Ng L, Lau C *et al.* Allen brain atlas: an integrated spatio-temporal portal for exploring the central nervous system. *Nucleic Acids Res* 2013;**41**:D996–1008. https://doi.org/10.1093/nar/gks1042
31. Gilmore EC, Herrup K. Cortical development: layers of complexity. *Curr Biol* 1997;**7**:R231–4. https://doi.org/10.1016/S0960-9822(06)00108-4
32. Larsen DD, Callaway EM. Development of layer-specific axonal arborizations in mouse primary somatosensory cortex. *J Comp Neurol* 2006;**494**:398–414.
33. Dimitrov D, Türei D, Garrido-Rodriguez M *et al.* Comparison of methods and resources for cell-cell communication inference from single-cell RNA-Seq data. *Nat Commun* 2022;**13**:3224. https://doi.org/10.1038/s41467-022-30755-0
34. Waylen LN, Nim HT, Martelotto LG *et al.* From whole-mount to single-cell spatial assessment of gene expression in 3D. *Commun Biol* 2020;**3**:602. https://doi.org/10.1038/s42003-020-01341-1
35. Lohoff T, Ghazanfar S, Missarova A *et al.* Integration of spatial and single-cell transcriptomic data elucidates mouse organogenesis. *Nat Biotechnol* 2022;**40**:74–85. https://doi.org/10.1038/s41587-021-01006-2
36. Asp M, Giacomello S, Larsson L *et al.* A spatiotemporal organ-wide gene expression and cell atlas of the developing human heart. *Cell* 2019;**179**:1647–1660.e19. https://doi.org/10.1016/j.cell.2019.11.025
37. Stahl PL, Salmén F, Vickovic S *et al.* Visualization and analysis of gene expression in tissue sections by spatial transcriptomics. *Science* 2016;**353**:78–82. https://doi.org/10.1126/science.aaf2403
38. Salmen F, Ståhl PL, Mollbrink A *et al.* Barcoded solid-phase RNA capture for spatial transcriptomics profiling in mammalian tissue sections. *Nat Protoc* 2018;**13**:2501–34. https://doi.org/10.1038/s41596-018-0045-2
39. Brade T, Pane LS, Moretti A *et al.* Embryonic heart progenitors and cardiogenesis. *Cold Spring Harb Perspect Med* 2013;**3**:a013847. https://doi.org/10.1101/cshperspect.a013847
40. Buckingham M, Meilhac S, Zaffran S. Building the mammalian heart from two sources of myocardial cells. *Nat Rev Genet* 2005;**6**:826–35.
41. Evans SM, Yelon D, Conlon FL *et al.* Myocardial lineage development. *Circ Res* 2010;**107**:1428–44.
42. Miquerol L, Kelly RG. Organogenesis of the vertebrate heart. *Wiley Interdiscip Rev Dev Biol* 2013;**2**:17–29. https://doi.org/10.1002/wdev.68
43. Anderson RH, Mori S, Spicer DE *et al.* Development and morphology of the ventricular outflow tracts. *World J Pediatr Congenit Heart Surg* 2016;**7**:561–77. https://doi.org/10.1177/2150135116651114
44. Sugishita Y, Watanabe M, Fisher SA. The development of the embryonic outflow tract provides novel insights into cardiac differentiation and remodeling. *Trends Cardiovasc Med* 2004;**14**:235–41.
45. Wu M. Mechanisms of trabecular formation and specification during Cardiogenesis. *Pediatr Cardiol* 2018;**39**:1082–9.
46. Sedmera D, Pexieder T, Vuillemin M *et al.* Developmental patterning of the myocardium. *Anat Rec* 2000;**258**:319–37.
47. Weiford BC, Subbarao VD, Mulhern KM. Noncompaction of the ventricular myocardium. *Circulation* 2004;**109**:2965–71.
48. Manasek FJ. Embryonic development of the heart. I. A light and electron microscopic study of myocardial development in the early chick embryo. *J Morphol* 1968;**125**:329–65.
49. Icardo JM, Fernandez-Teran A. Morphologic study of ventricular trabeculation in the embryonic chick heart. *Acta Anat (Basel)* 1987;**130**:264–74.
50. Wang M, Hu Q, Lv T *et al.* High-resolution 3D spatiotemporal transcriptomic maps of developing drosophila embryos and larvae. *Dev Cell* 2022;**57**:1271–1283.e4. https://doi.org/10.1016/j.devcel.2022.04.006
51. Daftary SS, Gore AC. The hypothalamic insulin-like growth factor-1 receptor and its relationship to gonadotropin-releasing hormones neurones during postnatal development. *J Neuroendocrinol* 2004;**16**:160–9.
52. Al-Samerria S, Radovick S. The role of insulin-like growth Factor-1 (IGF-1) in the control of neuroendocrine regulation of growth. *Cells* 2021;**10**:2664. https://doi.org/10.3390/cells10102664

53. Hashikawa K, Hashikawa Y, Tremblay R *et al.* Esr1(+) cells in the ventromedial hypothalamus control female aggression. *Nat Neurosci* 2017;**20**:1580–90. https://doi.org/10.1038/nn.4644
54. Lo L, Yao S, Kim DW *et al.* Connectional architecture of a mouse hypothalamic circuit node controlling social behavior. *Proc Natl Acad Sci USA* 2019;**116**:7503–12. https://doi.org/10.1073/pnas.1817503116
55. Zempo B, Karigo T, Kanda S *et al.* Morphological analysis of the axonal projections of EGFP-Labeled Esr1-expressing neurons in transgenic female medaka. *Endocrinology* 2018;**159**:1228–41.
56. Steuernagel L, Lam BYH, Klemm P *et al.* HypoMap-a unified single-cell gene expression atlas of the murine hypothalamus. *Nat Metab* 2022;**4**:1402–19. https://doi.org/10.1038/s42255-022-00657-y
57. Yang HP, Wang L, Han L *et al.* Nonsocial functions of hypothalamic oxytocin. *ISRN Neurosci* 2013;**2013**:179272. https://doi.org/10.1155/2013/179272
58. Madrigal MP, Jurado S. Specification of oxytocinergic and vasopressinergic circuits in the developing mouse brain. *Commun Biol* 2021;**4**:586. https://doi.org/10.1038/s42003-021-02110-4
59. Wang Y, Eddison M, Fleishman G *et al.* EASI-FISH for thick tissue defines lateral hypothalamus spatio-molecular organization. *Cell* 2021;**184**:6361–6377.e24. https://doi.org/10.1016/j.cell.2021.11.024
60. Xu S, Zhang Y, Pham D *et al.* Antileakage Fourier transform for seismic data regularization. *Geophysics* 2005;**70**:87–95.
61. Xu S, Zhang Y, Lambaré G. Antileakage Fourier transform for seismic data regularization in higher dimensions. *Geophysics* 2010;**75**:113–20.
62. Tang C, McMechan GA. Combining multidirectional source vector with antitruncation-artifact Fourier transform to calculate angle gathers from reverse time migration in two steps. *Geophysics* 2017;**82**:359–76.
63. Kipf TN, Welling M. Semi-Supervised Classification with Graph Convolutional Networks. In: Lorget T. (ed.), *5th International Conference on Learning Representations (ICLR).* (Vol. **2017**, pp. 1–14). 2017, Amherst, MA: JMLR Inc. and Microtome Publishing.
64. Xie J, Girshick R, Farhadi A. Unsupervised Deep Embedding for Clustering Analysis. In: *Proceedings of the 33rd International Conference on Machine Learning* (Vol. *48*, pp. 478–487), 2016. Brookline, MA: JMLR Inc. and Microtome Publishing.
65. Ren H, Walker BL, Cang Z *et al.* Identifying multicellular spatiotemporal organization of cells with SpaceFlow. *Nat Commun* 2022;**13**:4076. https://doi.org/10.1038/s41467-022-31739-w

Briefings in Bioinformatics, 2026, **27**, bbag060
https://doi.org/10.1093/bib/bbag060
Problem Solving Protocol